

# Alexandrina Untaroiu<sup>1</sup>

Department of Mechanical Engineering, Virginia Tech, Norris Hall, Room 324, 495 Old Turner Street, Blacksburg, VA 24061 e-mail: alexu@vt.edu

# S. M. Mahbobur Rahman

Department of Mechanical Engineering, Virginia Tech, Norris Hall, Room 107, 495 Old Turner Street Blacksburg, VA 24061 e-mail: mahbobur@vt.edu

# Christopher R. Martin

Department of Mechanical Engineering, Altoona College, Penn State University, Eiche Library, Room 145, Ivyside Park, Altoona, PA 3000 e-mail: crm28@psu.edu

# Role of Secondary Ions on the *i-v* Characteristics of Oxyfuel Flame Subject to an Electric Field

Recent use of ion currents as a sensing strategy in the mechanized oxyfuel cutting process motivated a series of studies which revealed that the steel work piece contributes secondary ions in addition to the primary ions classically identified in the oxyfuel flame. In this work, we present a computational model that has linked carbon-related chemi-ions as a source of secondary ions in preheating stage of oxyfuel cutting process subject to electric bias voltages. The flames' response to the electric field at different positive and negative polarities manifested a better understanding of the physical behavior of current-voltage (i-v) relationship. While copper surface exhibits stable and repeatable i-v characteristics, sporadically enhanced current was observed in positive saturation regime for steel surface, and this is believed to be due to the presence of secondary chemi-ions. To this extent, a source term of gaseous carbon has been assigned to mimic the 'work surface' reactions. The hypothesis is that since carbon is an important element, it will be diffusing out of the steel surface and evaporate into the flame. [DOI: 10.1115/1.4056845]

Keywords: oxyfuel flame, electric field, CFD, carbon, secondary ions, i-v characteristics

### Introduction

This work presents a computational model that investigates the role of secondary ions in oxyfuel cutting process at preheating stage. Oxyfuel flame cutting is a century-old technique having widespread applications in heavy industries due to its low cost and unparalleled performance on metal surfaces. In this process, the cutting torches use premixed oxygen-fuel gas mixture to heat metallic work pieces, so they can be cut chemically by a high-speed jet of pure oxygen. A pictorial view of the preheating process in oxyfuel flame cutting is shown in Fig. 1. The work piece (d) is brought to a kindling temperature by means of a preheat flame (c), and no cutting oxygen (b) is applied in this stage.

However, the mechanized oxyfuel-cutting process has never benefited from the degree of autonomy due to contemporary sensing technologies' limitations at high-temperature working conditions. A potential solution to this problem is motivated by preliminary measurements demonstrating that electrical events called 'ion currents' associated with the flame itself can reliably indicate vital process states.

It has been well established that high-temperature reaction zones in flames conduct electricity due to the chemi-ionization process [1,2]. Prior works in the literature [3–5] indicated the current–voltage (i- $\nu$ ) relationship with different critical parameters (such as standoff, flowrate, fuel-oxygen ratio, etc.) of oxyfuel flame to be the salient electrical characteristic under electric field in the preheating process. Demonstrably, when a voltage is applied between the torch and work piece, the i- $\nu$  curve adopts three distinct regimes [6]. Moreover, the i- $\nu$  curves have been further investigated to elucidate the production rate of charged species [7,8], and the effect of electric fields on flames [9–12]. Much work was dedicated in the late twentieth century toward identifying the chemical mechanisms for the formation and recombination of these ions in flames [2,13,14], revealing that carbon-bearing fuels produce ions,  $H_3O^+$  as a dominant cation.

A comprehensive two-dimensional computational simulation only with the reduced combustion chemical mechanism with ion-exchange reactions has already been completed [15] to elucidate the experimental results and to investigate the electrical characteristics such as ion migrations and ion distributions. Nonetheless, the findings exhibit some magnitude of differences compared to the experimental results [6,11]. In Ref. [6], study of ion currents in the oxyfuel cutting system revealed that there are two sources of ions; primary ions that are generated in the flame itself and secondary ions that are generated at the work piece. The work unveiled that, "copper work pieces have stable and repeatable i- $\nu$  characteristics regardless of the metal temperature. Meanwhile, i- $\nu$  characteristics over steel work pieces were found to exhibit an unrepeatable enhanced current in positive voltage regime and drift in the floating potential."

The secondary ions are generated chemically at the work surface; however, the mechanisms of their origin are yet to unfold. Surface chemical activity is imperative in materials other than metal catalysts. Much work has been carried out to demonstrate the sensitivity of surface kinetics [16,17]. The measurements presented here are designed to identify the dominant processes in a physical system and provide the empirical justification that is necessary for formulating a robust numerical model. Furthermore, depending on the surface material and wall temperature, chemical effects can differ [18,19]. Vlachos et al. numerically investigated the effects of radical removal by means of surface reaction on the H<sub>2</sub>-air and CH<sub>4</sub>-air premixed flames [20,21]. It was observed that adsorption reactions of OH, O, H, and CH<sub>3</sub> significantly influence extinction in methane-air combustion. Most recently, Narukawa et al. [22] and Salimath et al. [23] performed direct numerical simulations (DNS) of premixed flames impinging on the wall surface to investigate the near-wall flame behavior considering surface chemical activity. However, these investigations do not establish a sound explanation for the sporadically enhanced current in the positive regime of the i-v curve. In our latest experimental investigation [24], carbon contained in steel has been identified as an important source of secondary ions in the oxyfuel-cutting process. In addition, it was observed that the carbon content in steel burned in the oxyfuel flame is directly linked to enhanced electrical currents.

Corresponding author.

Contributed by the Fluids Engineering Division of ASME for publication in the JOURNAL OF FLUIDS ENGINEERING. Manuscript received September 21, 2022; final manuscript received January 21, 2023; published online March 20, 2023. Assoc. Editor: Ehsan Roohi.

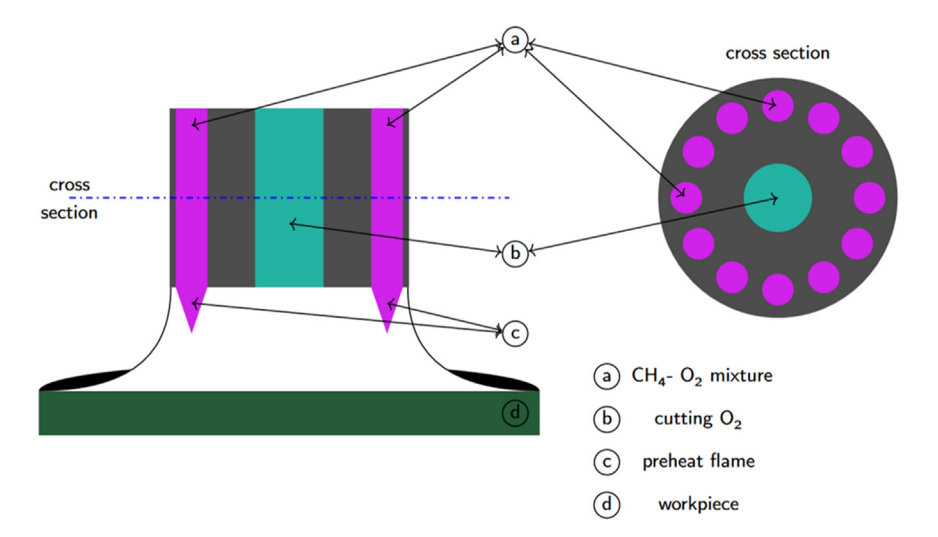


Fig. 1 Preheating of oxyfuel flame cutting process

The motivation for the present work stems from two main observations. First, although numerical and experimental studies on premixed flame have been performed extensively, limited research has been conducted to better understand the underlying physics. It is therefore of a great interest to generate a better understanding of the physical behavior of the oxyfuel-cutting flames, along with a more validated current-voltage (i-v) relationship. The second observation is the fact that carbon plays a critical role in the formation of ions in the flame [2]. Thereby, based on the experimental results that have sprung recently [24], we can exploit the methodology in a computational setup to elucidate the importance of the presence of carbon at the work piece.

The objective of the present work, therefore, is to develop an efficient computational model to elucidate the role of secondary ions due to carbon in oxyfuel flame cutting and to evaluate and quantify the electrical characteristics of this approach while also highlighting the fundamental differences between the numerical and experimental results. To support this objective, we create a source term of gaseous carbon to mimic the 'work surface' reactions. The hypothesis is that since carbon is an important element, it will be diffusing out of the work surface (steel) and evaporating into the flame. Once in the flame, pure carbon will react very quickly to form ions.

### **Materials and Methods**

The mole fractions of electrons and ions are infinitesimal with a maximum magnitude of  $\approx \! 10^{-7}$  in the flow. Therefore, under low voltage, the velocity and temperature profiles of the flow are barely affected by the transportation of electrons and ions [25]. Once the temperature and velocity profiles are calculated along with the generation rates of electrons and ions, the electrochemical species transport equations come into play to evaluate the transportation of electrons and ions. This further provides the electron and ion number densities together with the electric potential of the 2D domain. Concurrently, the electrochemical species transportation and recombination illustrate the electron and ion current densities.

**Geometry.** A simplified two-dimensional geometry as shown in Fig. 2 was considered to replicate the experimental setup [6]. As can be seen from the figure, we take advantage of the axial-symmetry of the system and therefore, considered only half of the physical setup and part of the work surface. Surfaces 1, 2, 7, 8, and 9 represent the torch tip on the whole, while surface 1 corresponds to an imaginary annular slot through which the premixed fuel-oxygen mixture is delivered. In this work, we present the

preheating process with a stable  $CH_4$ – $O_2$  mixture. The torch is made from either copper or steel and has a fixed distance of 12.7 mm ( $\approx 0.5$  in) above the work surface. This is often referred to as standoff distance.

Surface 3 represents the symmetry plane of the assembly, while surface 4 represents the work surface. Surface 4 has a width of 22 mm, with a vertical distance of 12.7 mm from surface 8. Rest surfaces are prescribed as wall boundary conditions, while surfaces 5 and 6 are treated as openings.

**Initial and Boundary Conditions.** The initial conditions for the 2D model are summarized in Table 1. Essentially, the model is initialized through standard air composition at a pressure of 1 atm and a temperature of 300 K.

The boundary conditions tabulated in Table 2 are chosen to be consistent with the experimental demonstration by Martin et al. [6,11]. The inlet velocity of the fuel oxygen mixture is  $12 \text{ ms}^{-1}$  with an inlet temperature of 600 K. Fuel-oxygen (F/O) ratio for this study is 0.833 which can be defined by specifying the mole fractions. Therefore, the mole fractions at inlet are  $\chi_{CH_4} = 0.45$  (fuel), and  $\chi_{O_2} = 0.55$ . The flowrate in the experimental investigation was 21 scfh [11], i.e., standard cubic feet per hour at a temperature of 288.15 K. Therefore, to provide an apple-to-apple comparison, the inlet velocity needs to be approximated for running the simulations. For this purpose, we consider one section of the preheat fuel outlet, i.e., one torch outlet, and calculate the area of that section. The torch outlets have a shape close to a triangle [26] and thus the area is found to be  $0.51 \text{ mm}^2$ . With the flowrate and area being known, the velocity is then approximated as

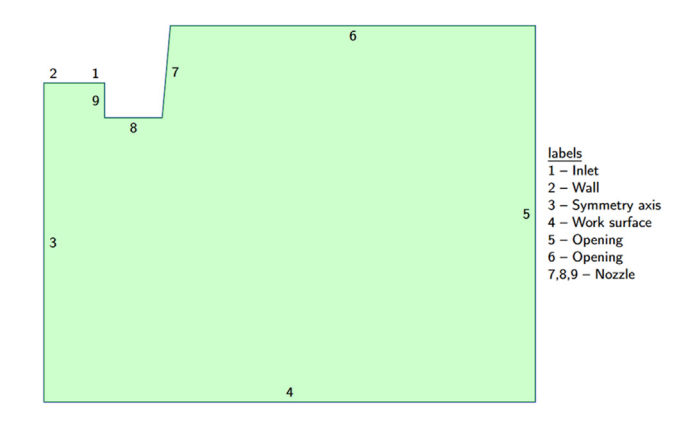


Fig. 2 2D model for the study

Table 1 Initial conditions for the computational model

Initial conditions	Physics values	
Static temperature	300 K	
Pressure	1 atm	
Velocity	$0{\rm ms}^{-1}$	
Mole fraction (γ)	$\chi_{O_2} = 0.23, \chi_{N_2} = 0.7565$	
Mole fraction (γ)	$\gamma_{CO_2} = 0.0005, \gamma_{Ar} = 0.01$	
Molar concentration	$\chi_{CO_2} = 0.0005, \chi_{Ar} = 0.01$ 0 Kmol/m <sup>3</sup>	
Electric potential	0V	

Parameters
 Physics value
 Ref.

 Temperature
 600 K

 Mole fraction, 
$$χ_{CH_4}$$
 0.45

 Mole fraction,  $χ_{O_2}$ 
 0.55

 Flame width
 1.5 mm

 Dynamic viscosity,  $μ_{mix}$ 
 1.7822 × 10<sup>-5</sup> Pa · s
 [31]

 Density,  $ρ_{mix}$ 
 1.008 kg/m³
 [31]

 Turbulence length scale, I
 1 × 10<sup>-3</sup> m
 [32]

Turbulence length scale, I

Table 3 Calculation parameters

$$U = \frac{Q}{12A} \tag{1}$$

where Q is the volumetric flowrate and A denotes the area of the triangular region. The number 12 on the denominator accounts for the fact that there are 12 small triangular torch outlets.

The work surface temperature is assigned to be 600 K, which is consistent with the preheating process from the experiment [11]. The torch surface is also considered to be at the same temperature, i.e., 600 K, however with a variation in electric potential applied. Since both the torch tip and the work piece are absorbing surfaces, the number density boundary conditions will be zero,  $n_e$  (0) =  $n_e$  $(L) = n_i(0) = n_i(L) = 0$ . The subscripts e and i correspond to electrons and ions, respectively. While some voltage,  $V_a$  is imposed at the torch, the work surface is assumed to be at ground potential. Therefore,  $V(0) = V_a \in [-10V, +10V], V(L) = 0.$ 

Lastly, for the turbulence model, the turbulent intensity is set as 0.5 along with a turbulent length scale value of 0.001 m. Overall, detailed summary of the boundary conditions for the current study is shown in Table 2.

Flame Type. Borghi Diagram [27] is used to determine the flame's physical behavior. The primary parameters to locate the flame type regime are: turbulent intensity (u'), laminar flame speed  $(S_{\rm L})$ , integral turbulence length (*l*), and laminar flame thickness ( $l_{\rm F}$ ). The laminar flame thickness,  $l_F$  is defined as

$$l_F = \frac{D}{S_L} \tag{2}$$

where the D is the molecular diffusion rate, and is related to the Schmidt number (c) and kinematic viscosity (v) through the following expression

$$Sc = \frac{\nu}{D} \tag{3}$$

It has been established [28,29] that for a general methane- air mixture,  $S_L$  is 0.4 ms<sup>-1</sup>, whereas the laminar methane oxygen flame speed is  $\approx 1.0 \, \mathrm{ms}^{-1}$ . Cantera [30] integrated in Python was employed to calculate the laminar flame speed for this study. With the parameters defined in Table 3,  $S_L$  for the current study is found to be  $4.5 \text{ ms}^{-1}$ .

Next, Mass-weighted mixture method is adopted to calculate the dynamic viscosity of the methane-oxygen mixture along with the density of the same

$$\mu = \sum_{i=1}^{N} Y_i \mu_i \tag{4}$$

[32]

$$\rho_{\text{avg.}} = \sum_{i=1}^{N} \chi_i \rho_i \tag{5}$$

where,  $Y_i$  is the mass fraction,  $\chi_i$  is the mole fraction,  $\mu_i$  is the viscosity,  $\rho_i$  is the density of component i, respectively. N is the mixtures' total number of components. The calculated values for both  $\mu$  and  $\rho$  for the mixture are shown in Table 3. With these values, the kinematic viscosity is then calculated by Eq. (6) and the value obtained is  $1.768056 \times 10^{-5}$  m

$$\nu = \frac{\mu}{\rho} \tag{6}$$

Successively, the molecular diffusion rate, D is then computed to be  $1.768056 \times 10^{-5}$  m for a Schmidt number of 1.0 [27] by Eq. (3). Then, with the know values for D and  $S_L$ , the flame thickness,  $l_{\rm F}$  is found to be  $3.929 \times 10^{-6}$  m. Finally, the turbulent intensity (u') is chosen to be 0.5%.

Now that all the variables have been enumerated, the ratios  $l/l_F$  and  $u'/S_L$  are then assessed. The 'green square' in Fig. 3 illustrates our present study which has a value of ≈ 255 along the x-axis  $(l/l_F)$  and  $\approx 12.5$  along y-axis  $(u'/S_L)$ . It is observed that

Table 2 Boundary conditions for the computational model

Boundary conditions	Momentum	Energy	Species	Potential
Inlet	$U = 12  \text{ms}^{-1}$	T = 600  K	$\chi_{CH_4} = 0.45,  \chi_{O_2} = 0.55$	[-10V, +10V]
Wall	$U\!=\!0ms^{-1}$	$T = 600 \mathrm{K}$	$-D\frac{dc}{dx} = 0$	[-10V, +10V]
Axial symmetry	_	_	_	_
Wall	$U=0ms^{-1}$	$T = 600 \mathrm{K}$	$-D\frac{dc}{dx} = 0$	0V
Opening	Outlet vent	_	$\chi_{N_2} = 0.781, \chi_{O_2} = 0.209$	_
Opening	Outlet vent	_	$\chi_{N_2} = 0.781, \chi_{O_2} = 0.209$	_
Wall	$U\!=\!0ms^{-1}$	$T = 600 \mathrm{K}$	$-D\frac{dc}{dx} = 0$	[-10V, +10V]
Wall	$U\!=\!0ms^{-1}$	$T = 600 \mathrm{K}$	$-D\frac{dc}{dx} = 0$	[-10V, +10V]
Wall	$U=0ms^{-1}$	$T = 600 \mathrm{K}$	$-D\frac{dc}{dx} = 0$	[-10V, +10V]
	Inlet Wall Axial symmetry Wall Opening Opening Wall Wall	Inlet $U = 12 \text{ ms}^{-1}$ Wall $U = 0 \text{ ms}^{-1}$ Axial symmetry —  Wall $U = 0 \text{ ms}^{-1}$ Opening Outlet vent  Opening Outlet vent  Wall $U = 0 \text{ ms}^{-1}$ Wall $U = 0 \text{ ms}^{-1}$	Inlet $U = 12  \text{ms}^{-1}$ $T = 600  \text{K}$ Wall $U = 0  \text{ms}^{-1}$ $T = 600  \text{K}$ Axial symmetry — — —  Wall $U = 0  \text{ms}^{-1}$ $T = 600  \text{K}$ Opening Outlet vent —  Opening Outlet vent — —  Wall $U = 0  \text{ms}^{-1}$ $T = 600  \text{K}$ Wall $U = 0  \text{ms}^{-1}$ $T = 600  \text{K}$	Inlet $U = 12 \mathrm{ms}^{-1}$ $T = 600 \mathrm{K}$ $\chi_{CH_4} = 0.45,  \chi_{O_2} = 0.55$ Wall $U = 0 \mathrm{ms}^{-1}$ $T = 600 \mathrm{K}$ $-D \frac{dc}{dx} = 0$ Axial symmetry — — — — — — — — — — — — — — — — — — —

the final value of our current study falls within the thin reaction zone in the Borghi diagram. Peters [27] demonstrated that when the flame is in the thin reaction zone, the preheat region of the flame will be bordered by turbulence. As such, to model the oxyfuel flame preheat phase, turbulence models are employed in the computational setup rather treating the flame regime as laminar.

Prior studies [33–35] have revealed that turbulent flame speed  $(S_T)$  can be correlated to the laminar flame speed  $(S_L)$  through a power-law function of the form

$$\frac{S_T}{S_I} \propto a \left(\frac{u'}{S_I}\right)^n$$
 (7)

Governing Equations. Flame modeling under the bias of electric voltage is governed by the conservation equations for reacting flows. The governing equations of the two-dimensional model involve the conservation of mass, momentum, energy, and species conservation equations, respectively, written as [36,37]

$$\frac{\partial \rho}{\partial t} + \nabla \cdot (\rho U) = 0 \tag{8}$$

$$\frac{\partial(\rho U)}{\partial t} + \nabla \cdot [\rho U \otimes U] = -\nabla \mathbf{p} + \nabla \cdot \overline{\overline{\tau}} + \rho \sum_{i}^{N} Y_{i} f_{i} \qquad (9)$$

$$\frac{\partial(\rho E)}{\partial t} + \nabla \cdot [(\rho E + p)U + \dot{q}] = \nabla \cdot (\overline{\overline{\tau}} \cdot \mathbf{U}) - \sum_{i}^{N} h_{i} \dot{\omega}_{i} + \rho \sum_{i}^{N} Y_{i} f_{i} \cdot (U + v_{i})$$
 (10)

$$\frac{\partial(\rho Y_i)}{\partial t} + \nabla \cdot [\rho(U - v_i)Y_i] = -\nabla \cdot J_i + R_i + S_i$$
 (11)

Equations (8)–(11) are solved for the density,  $\rho$ , the velocity vector, U, the total energy, E, and the mass fraction,  $Y_i$  for N numbers of reacting species. Pressure,  $\rho$  is calculated by the equation of state since the gas in this study is considered as ideal gas.

$$\rho = \frac{p}{RT} \tag{12}$$

Heat flux,  $\dot{q}$  from Eq. (10) is calculated from Fourier's law.  $f_i$  is the resultant body force acting on species i. From Eq. (10),  $h_i$ ,  $\dot{\omega}_i$ ,

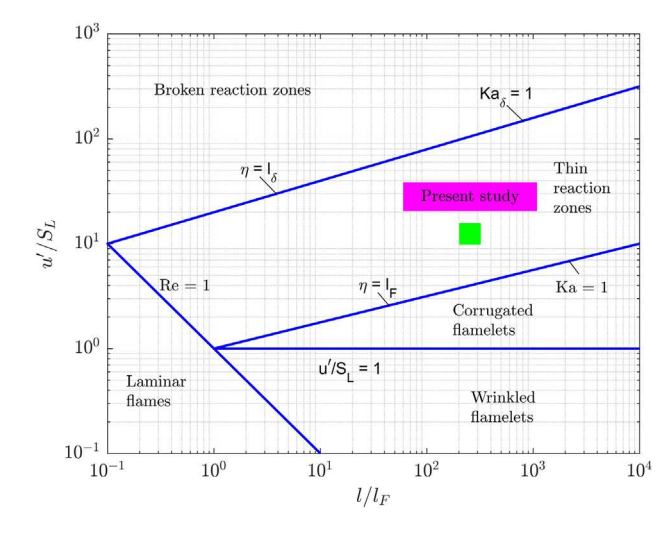


Fig. 3 Borghi diagram

and  $v_i$  are the enthalpy of formation, the molar source term, and the diffusion velocity of species i, respectively. I is the identity tensor and the stress tensor  $\tau$  is defined as

$$\overline{\overline{\tau}} = \left[ \left( \nabla U + \nabla U^T \right) - \frac{2}{3} \nabla \cdot U I \right] \tag{13}$$

The mass diffusion ( $J_i$  from Eq. (11)) in turbulent flows is computed by the following form

$$J_{i} = -\left(\rho D_{i,m} + \frac{\mu_{t}}{\rho D_{t}}\right) \nabla Y_{i} - D_{T,i} \frac{\nabla T}{T}$$
(14)

where  $Sc_t$  is the turbulent Schmidt number  $(=\frac{\mu_t}{\rho D_t})$ . Here,  $\mu_t$  is the turbulent viscosity and  $D_t$  is the turbulent diffusivity.

The flow inside the domain is turbulent in nature. For our study, we have adopted the realizable  $k-\varepsilon$  turbulence model [38], which combines the Boussinesq relationship [39] and the turbulent viscosity,  $\mu_t$ . Turbulent, or eddy viscosity is computed by combining k and  $\varepsilon$  as follows [37]:

$$\mu_t = \rho C_\mu \frac{k^2}{c} \tag{15}$$

where  $C\mu$  is a constant. The transport equations for k and  $\varepsilon$  in the realizable k- $\varepsilon$  model are

$$\frac{\partial}{\partial t}(\rho k) + \nabla \cdot (\rho k U) = \nabla \cdot \left[ \left( \mu + \frac{\mu_t}{\sigma_k} \right) \nabla k \right] + G_k + G_b - \rho \varepsilon$$
$$- Y_M + S_k$$

(16)

$$\frac{\partial}{\partial t}(\rho k) + \nabla \cdot (\rho \varepsilon U) = \nabla \cdot \left[ \left( \mu + \frac{\mu_t}{\sigma_{\varepsilon}} \right) \nabla \varepsilon \right] + \rho C_1 S \varepsilon 
- \rho C_2 \frac{\varepsilon^2}{k + \sqrt{\nu \varepsilon}} + C_{1\varepsilon} \frac{\varepsilon}{k} C_{3\varepsilon} G_b + S_{\varepsilon} \quad (17)$$

where

$$G_k = -\rho \overline{u_i' u_j'} \frac{\partial u_j}{\partial x_i}$$
 (18)

$$G_b = \beta g_i \frac{\mu_t}{Pr_t} \frac{\partial T}{\partial x_i} \tag{19}$$

$$Y_M = 2\rho \varepsilon M_t^2 \tag{20}$$

$$C_1 = \max \left[ 0.43, \frac{\eta}{\eta + 5} \right] \tag{21}$$

$$\eta = S \frac{k}{\varepsilon} \tag{22}$$

$$S = \sqrt{2S : S} \tag{23}$$

$$S = \frac{1}{2} (\nabla U + \nabla U^T) \tag{24}$$

In Eqs. (16)–(17),  $G_k$  represents the generation of turbulence kinetic energy due to the mean velocity gradients.  $G_b$  is the generation of turbulence kinetic energy due to buoyancy.  $Y_M$  represents the contribution of the fluctuating dilatation in compressible turbulence to the overall dissipation rate.  $C_2$  and  $C_{1\epsilon}$  (=1.44) are constants.  $\sigma_k$  (=1.0) and  $\sigma_\epsilon$  (=1.2) are the turbulent Prandtl

Table 4 Arrhenius parameters for the ionization reaction mechanisms

Reactions	Pre-exponential factor, A (cm³/mol·s)	Temperature dependence, $\beta$	Activation energy, E <sub>a</sub> (J/mol)
$CH + O \iff HCO^{+} + e^{-}$ $HCO^{+} + H_{2}O \iff H_{3}O^{+} + CO$ $H_{3}O^{+} + e^{-} \iff H_{2}O + H$	$\begin{array}{c} 2.512 \times 10^{11} \\ 1.0 \times 10^{16} \\ 1.44 \times 10^{17} \end{array}$	0 -0.0897 0	$7.118 \times 10^{3}$ 0 0

numbers for k and  $\varepsilon$ , respectively.  $S_k$  and  $S_{\varepsilon}$  are user-defined source terms. In Eq. (23), S is the modulus of mean strain rate tensor, S, which is defined by Eq. (24).

In addition, for the turbulent model, dimensionless wall distance, otherwise known as  $y^+$  value, is considered as an imperative parameter in models' convergence. The  $y^+$  value is defined as

$$y^+ \equiv \frac{u_* y}{\nu} \tag{25}$$

where y is the distance to the nearest wall and  $u_*$  is the friction velocity near the nearest wall which has the following form:

$$u_* \equiv \sqrt{\frac{\tau_\omega}{\rho}} \tag{26}$$

 $\tau_{\omega}$  is known as the wall shear stress.

Chemical Kinetic Mechanism. A chemical kinetic mechanism is required for the computational model that includes both neutral species and ionic species reactions. Through chemi-ionization, the mechanism should concede the production and depletion of ions. Additionally, ion-molecule reactions, and dissociative recombination should also be exerted by this mechanism.

In the current study, the reactions of the methane-oxygen  $(CH_4-O_2)$  flame are combined with GRI 3.0 [40] and additional ionization reactions from Belhi et al. [41] to describe the chemistry of ions in flames. The thermodynamic properties of the charged species are taken from Burcat database [42]. Table 4 presents the coefficients magnitudes [10] of the ionization reactions. The transport properties are extracted from a methane-air reaction presented by Chen et al. [43].

The reaction rates are calculated by the Arrhenius' equation, as follow:

$$k = AT^{\beta} e^{-\frac{E_{\alpha}}{R_{u}T}} \tag{27}$$

The recombination rate is calculated by equation

$$\frac{d[E]}{dt} = \frac{d[\text{ion}]}{dt} = -k \cdot [E][\text{ion}]$$
 (28)

The ions and electrons have a negligible effect on the flow under a low electric potential environment, and both the generation rate of ions and electrons are extracted from the model. The mobility of electrons is 0.2 m $^2$   $V^{-1}$  s $^{-1}$  [44] and 0.0018 m $^2$   $V^{-1}$  s $^{-1}$  for the ions [26], respectively. Nernst-Einstein relation is used to calculate the molecular diffusivity as follow:

$$D_i = \frac{k_i k_B T}{q_e} \tag{29}$$

where  $k_B$  is Boltzmann's constant, and  $q_e$  is the electrical charge of a particle. For the electrical characteristic analysis, since we only have a part of the work surface, the electric current density [15,45] is calculated through the following expressions

$$J_{\text{ion}} = -\sigma_{\text{ion}} K \nabla V - D \nabla \sigma_{\text{ion}} + \sigma_{\text{ion}} U$$
 (30)

$$J_e = \sigma_e K \nabla V - D \nabla \sigma_e + \sigma_e U \tag{31}$$

where  $\sigma_{\text{ion}}$  and  $\sigma_e$  are the space charge densities for ions and electrons, respectively, and are defined as

$$\sigma_{\rm ion} = q N_a c_{\rm ion} \tag{32}$$

$$\sigma_e = q N_a c_e \tag{33}$$

In Eqs. (32) and (33),  $N_a$  is the Avogadro constant,  $(=6.02214086\times10^{23}/\text{mol})$ ,  $c_{\text{ion}}$  is the molar concentration of ions, and  $c_e$  is the molar concentration of electrons. As can be seen, the electric current density is related to the electron species' mobility, diffusivity, space, and bulk velocity, whereas the ion charge density is determined based on the molar concentration of ion species.

Model Configuration and Computational Procedure. A 2D CFD model for the domain as shown in Fig. 2 was developed using ANSYS FLUENT 2020R2. Two different metallic surfaces, steel, and copper were considered as the work surface (surface 4) in the 2D model to imitate the experimental setup [6]. The material properties of both steel and copper are listed in Table 5. Furthermore, while considering the steel surface, a source term of gaseous carbon is assigned at surface 4 to mimic the 'work surface' reactions. In this approach, the combustible carbon element is assigned a definite mass flowrate of  $1.78 \times 10^{-5}$  kg/s based on the analytical expression employed in the experimental investigation,  $\dot{m} = \frac{\pi}{4} D^2 \rho \chi \mathcal{F}$  [24]. The reaction rates were then tracked at different radial flame lines using the modified Arrhenius' equation as shown in Ref. [10]. Carbon comprises for around 0.20% in low-carbon steel [46]. The hypothesis is that since carbon is an important element, it will be diffusing out of the work surface (steel) and evaporating into the flame. Once in the flame, pure carbon will react very quickly to form ions.

The governing equations are solved by employing a finite volume approach. Second-order spatial discretization scheme was adopted to discretize the governing equations in the whole domain. Moreover, coupled solution method and the coupled pressure–velocity coupling algorithm were used to solve the governing equations. The PRESTO! scheme designed for flows involving steep pressure gradients was chosen for the pressure equation. The realizable k– $\epsilon$  turbulence model was considered the viscous model. Stiff chemistry solver along with the eddy dissipation concept (EDC) was introduced to the CFD code to solve for the turbulence-chemistry interaction.

The eddy-dissipation-concept (EDC) model is an extension of the eddy-dissipation model to include detailed chemical

Table 5 Material properties

Properties	Value	Ref.	
Steel (AISI 1018)			
Density $(\rho)$	$7900  \text{kg/m}^3$	[ <mark>6</mark> ]	
Specific heat (c)	500 J/kg/K	[ <mark>6</mark> ]	
Thermal conductivity (k)	51.9 w/m ⋅ k	[47]	
Electrical conductivity $(\sigma)$	$3.413 \times 10^{+6} \text{ S/m}$	[48]	
Copper (ETP C110)			
Density $(\rho)$	$8890  \text{kg/m}^3$	[48]	
Specific heat (c)	385 J/kg/K	[48]	
Thermal conductivity (k)	300 w/m ⋅ k	[6]	
Electrical conductivity ( $\sigma$ )	$5.5249 \times 10^{+7}$ S/m	[48]	

mechanisms in turbulent flows [37]. For EDC model, the source term in the conservation equation for the mean species i, is modeled as

$$R_{i} = \frac{\rho(\xi^{*})^{2}}{\tau^{*} \left[1 - (\xi^{*})^{3}\right]} (Y_{i}^{*} - Y_{i})$$
(34)

where  $Y_i^*$  is the fine-scale species mass fraction after reacting over the time  $\tau^*$ .  $\tau^*$  is defined as

$$\tau^* = C_\tau \left(\frac{\nu}{\epsilon}\right)^{\frac{1}{2}} \tag{35}$$

where  $C_{\tau}$  is a time scale constant.

Moreover, the EDC assumes that reaction occurs in small turbulent structures, called the fine scales. The length fraction of the fine scales are modeled as

$$\xi^* = C_{\xi} \left( \frac{\nu \varepsilon}{k^2} \right)^{\frac{1}{4}} \tag{36}$$

where \* denotes fine-scale quantities and,  $C_{\xi}$  is the volume fraction constant, and  $\nu$  is the kinematic viscosity.

In Situ Adaptive Algorithm (ISAT) [37,49] was selected as the integration method for the chemistry solver since ISAT can accelerate the chemistry calculations by two to three orders of magnitude, thus offering substantial reductions in run-times. Finally, the convergence criterion requirement is set to be  $10\times10^{-6}$  as the residual term for the equations. The parameters for the current CFD setup are summarized in Table 6.

Simulations for the current computational model were carried out in one of the high-performance computing systems, 'TinkerCliffs', from the Advanced Research Computing (ARC) division at Virginia Tech. TinkerCliffs has an AMD EPYC 7702, Intel Xeon Platinum 9242 CPU model @ 2.0–2.3 GHz with 41,984 cores.

# **Results and Discussions**

For the purpose of lateral comparison, we create somewhat virtual flame inspection lines in the 2D domain as shown in Fig. 4. Another motivation to do so is the fact that the color schemes in such 2D model are difficult to analyze since the variation of magnitude of the number densities will be substantial.

As shown, we have three segmented vertical lines, and a horizontal line over surface 4. The vertical lines, in our case, the flame lines have a total length of  $\approx 14.25$  mm. Flame lines 1 and 3 have increased resolution along a distance of  $\approx 2$  mm from surfaces 1 and 4, respectively, meaning they are divided into much finer nodal points. This is done because the process parameters and electrical characteristics change rapidly depending on where you are in the flow, and these changes are very swift near surfaces 1 (torch/inlet area) and 4 (work surface). As such, another vertical

Table 6 Parameters in CFD setup

Initial conditions	Physics values	
2D space	Axisymmetric	
Chemistry solver	Stiff chemistry solver	
Turbulence-chemistry	Eddy dissipation concept	
Turbulence model	Realizable k-ε	
Turbulent intensity	0.5%	
Turbulent length scale	0.001 m	
Formulation	RANS	
Solver	Coupled, Incompressible	
Spatial discretization	Second-order	
Convergence criteria	$10 \times 10^{-6}$	

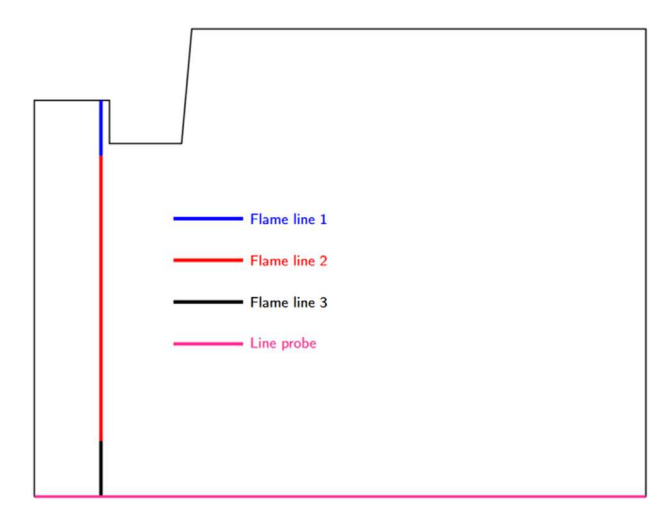


Fig. 4 Flame inspection lines to extract postprocess results

line, a line probe, is also considered which is  $\approx 5.5\,\mathrm{mm}$  above the work surface.

All things considered, the results presented herein are extracted along these flame lines, if not indicated otherwise. Furthermore, they also act as the axial and radial distribution lines for the current 2D analysis. Furthermore, the results are discussed through combustion part (Temperature, velocity, etc.) and subsequent eletrochemical part, to impart a sound understanding.

**Temperature and Velocity Distribution.** The temperature contour plot near the torch tip for the two-dimensional domain is shown in Fig. 5. The geometry of the flame is characterized with having 'inner' and 'outer' cones that describe the luminous zone formation at the front.

As shown, the premixed methane-oxygen flame generated in the two-dimensional domain has a V-shaped flame. The profile also illustrates that the temperature is high beneath the V-shape slit. According to Nernst–Einstein equation, the electrons and ions will have a high diffusion rate. Additionally, the profile of temperature at the reaction zone changes [31] for accounting turbulence.

Furthermore, the axially distributed temperature profile as shown in Fig. 6 illustrates that at flame front ( $\approx 5.7$  mm), where the mixture of fuel (CH<sub>4</sub>) and air (O<sub>2</sub>) are well premixed, the temperature is maximum.

The radial velocity is much more comprehensible than the axial velocity in the flow for a two-dimensional flame, and the phenomena are shown in Fig. 7. The velocity declines over a 1 mm length scale close to the work surface. At a sufficiently high voltage, the flow field can be shifted toward the electric bias areas.

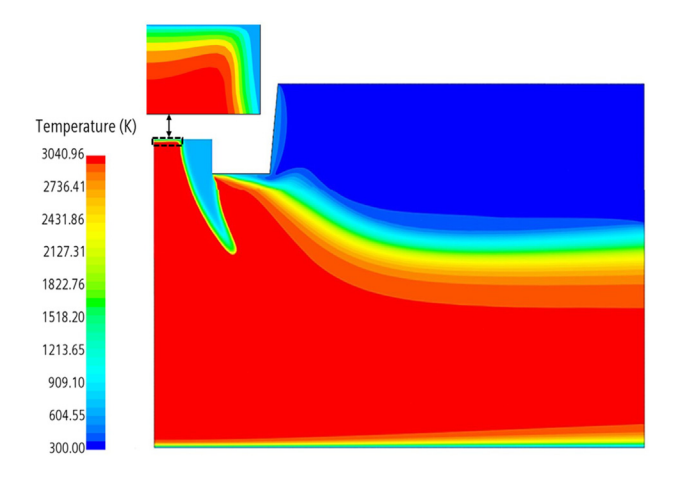


Fig. 5 Temperature contour plot near the torch tip

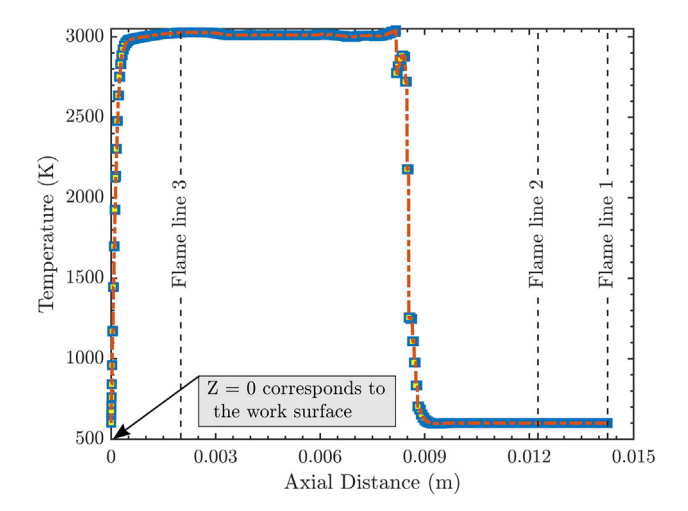


Fig. 6 Axially distributed Temperature profile

As indicated in chemical kinetic mechanism, Hydronium  $(H_3O^+)$  and formyl  $(HCO^+)$  cations are the two ions in the ionization reactions with  $H_3O^+$  ion being the abundant one [50]. The generation rate of  $H_3O^+$  is as good as that of the electrons  $(e^-)$ , whereas  $HCO^+$  has a substantially lower generation rate.

**Number Density.** When a sufficiently strong electric bias voltage is applied, the charge carriers can be driven away to the vicinity of the absorbing surfaces. Boucher [51] experimentally confirmed that the metal surfaces absorb free electrons due to their rapid transport in the gas phase and produce a positively charged 'sheath'.

The electrical species transport model results in the number density profiles of electrons and ions. The axial distribution of the number densities for both  $\rm H_3O^+$  and  $\rm e^-$  are shown in Fig. 8. This is done since the two-dimensional color scheme is difficult to analyze as the magnitude of the densities changes extensively. The magnitudes change very rapidly near the surfaces (inlet and work surfaces). As can be seen from Fig. 8, the maximum magnitude of species number density is  $10^{18}/m3$ , and this tones with the physical measurement [26]. The sheaths' saturation can be observed by constraining the torch and work surface number densities boundary condition to zero. The electrons' (e<sup>-</sup>) and ions' ( $\rm H_3O^+$ ) number densities peak at the flame front which is  $\approx 5.7$  mm. Figures 8(a)-8(c) provides pictorial illustration of the number densities at different electric bias voltages and are discussed below:

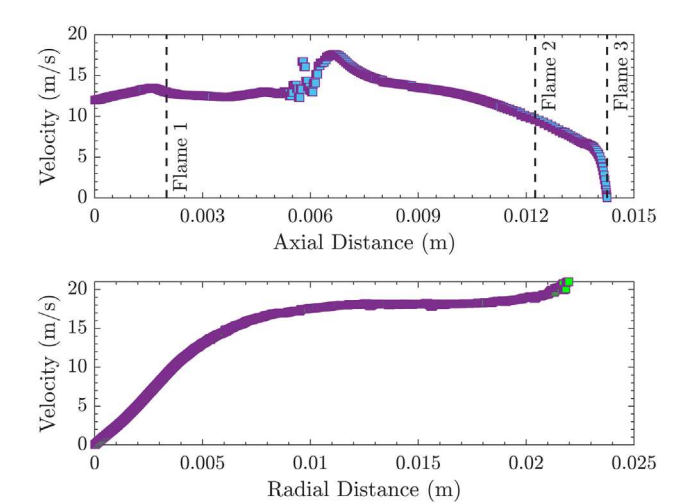


Fig. 7 Axial and radial Velocity distribution

- (i) When a voltage of -10V is applied at the torch, we can observe a swift increase in the number of ions (H<sub>3</sub>O<sup>+</sup>) at the torch surface which vanishes more rapidly at the work surface than the electrons (e<sup>-</sup>). Even though the applied voltage is driving them (e<sup>-</sup>) in that direction, e<sup>-</sup> vanishes almost entirely at the work surface. This is the formation of a 'sheath'.
- (ii) Things become a bit interesting when a torch voltage of 0V is applied as shown in Fig. 8(b). In this case, there is a slow expansion of H<sub>3</sub>O<sup>+</sup> at the beginning of the torch tip surface, while the increment of the number of e<sup>-</sup> is swift. The radial velocity leads electrons away. However, e<sup>-</sup> disappear quickly at the work surface than H<sub>3</sub>O<sup>+</sup>. The charge carrier pair of H<sub>3</sub>O<sup>+</sup> and e<sup>-</sup> differs in mass by some 35 thousand times [6]. In addition, the heavy positive ions are in the power of bulk fluid velocity, whereas the tiny electrons respond to the electric field and are at liberty to diffuse. Thence, the electrons move more comfortably than the ions in CH<sub>4</sub>-O<sub>2</sub> flame. Sheaths are formed in both surfaces (torch and work surface) because of the number of differences between ions and electrons, suggesting that the grid was able to resolve the Debye length.
- (iii) Figure 8(c) corresponds to the number densities of  $H_3O^+$  and  $e^-$  when a torch electric bias voltage of +10V is applied. In contrast to the -10V case, when a positive electric bias is applied, +10V in this case, there is a swift increase in number densities of  $e^-$  at the torch surface, whereas they vanish quickly at the work surface. Simultaneously, the ions  $(H_3O^+)$  start to dwindle at the torch surface with an abrupt drop at around 1.8 mm. This is where the torch ends, and a radial velocity appears. Nonetheless,  $H_3O^+$  ions remain significant at the work surface.

**Electric Potential.** It has been established that a mixture-average approach with potentials adequate for charged species is appropriate for modeling ion-transport [52]. The electric potential (V) can be defined through the electric field vector (E) by Gauss law as

$$-\nabla \cdot \mathbf{E} = -\nabla^2 V = \frac{\sum_i q_i e n_i}{\epsilon_0}$$
 (37)

where  $q_i$  and  $n_i$  are the charge number and the number density of species i, respectively.  $\epsilon_0$  is the permittivity of free space and is equal to  $8.8542 \times 10^{12}$  farad/m.

The electric potential for three different voltages,  $-10\,\mathrm{V}$ ,  $0\,\mathrm{V}$ , and  $+10\,\mathrm{V}$  are shown in Fig. 9. These are plotted axially along the flame line once the number density of electrons and ions has been calculated. It can be observed that even though an electric bias voltage of  $0\,\mathrm{V}$  is applied, due to sheaths' charge accumulation, the electrical potential rises above  $0\,\mathrm{V}$ . When a positive voltage  $(+10\,\mathrm{V})$  or relatively strong electric potential is applied, the concentration of negative ions becomes insignificant. This leads to one of the sheaths dominating as electrons evacuate quickly leaving a positive charge in their wake. However, negative ions are dominant when a negative voltage of  $-10\,\mathrm{V}$  is applied. Due to 'ohmic losses' along the flame's length, a significant voltage drop can be observed in Fig. 9.

The contour plots for the electric potential over the domain are shown in Figs. 10(a) and 10(b) for  $+10\,\mathrm{V}$  and  $-10\,\mathrm{V}$ , respectively. These plots also illustrate the differences between positive and negative torch surface potential. Belhi et al. [45] described that charged species are driven by the local gradient of the electric potential when an electric field is applied. In this way, the positive charges are transported from the reaction zone and negative charges move in the opposite direction. It is evident from Fig. 10 that in both figures the flame is nearly uniform in potential. The flame front is much more electrically conductive because of the high density of ions there. Considering Fig. 10(a) as an instance,

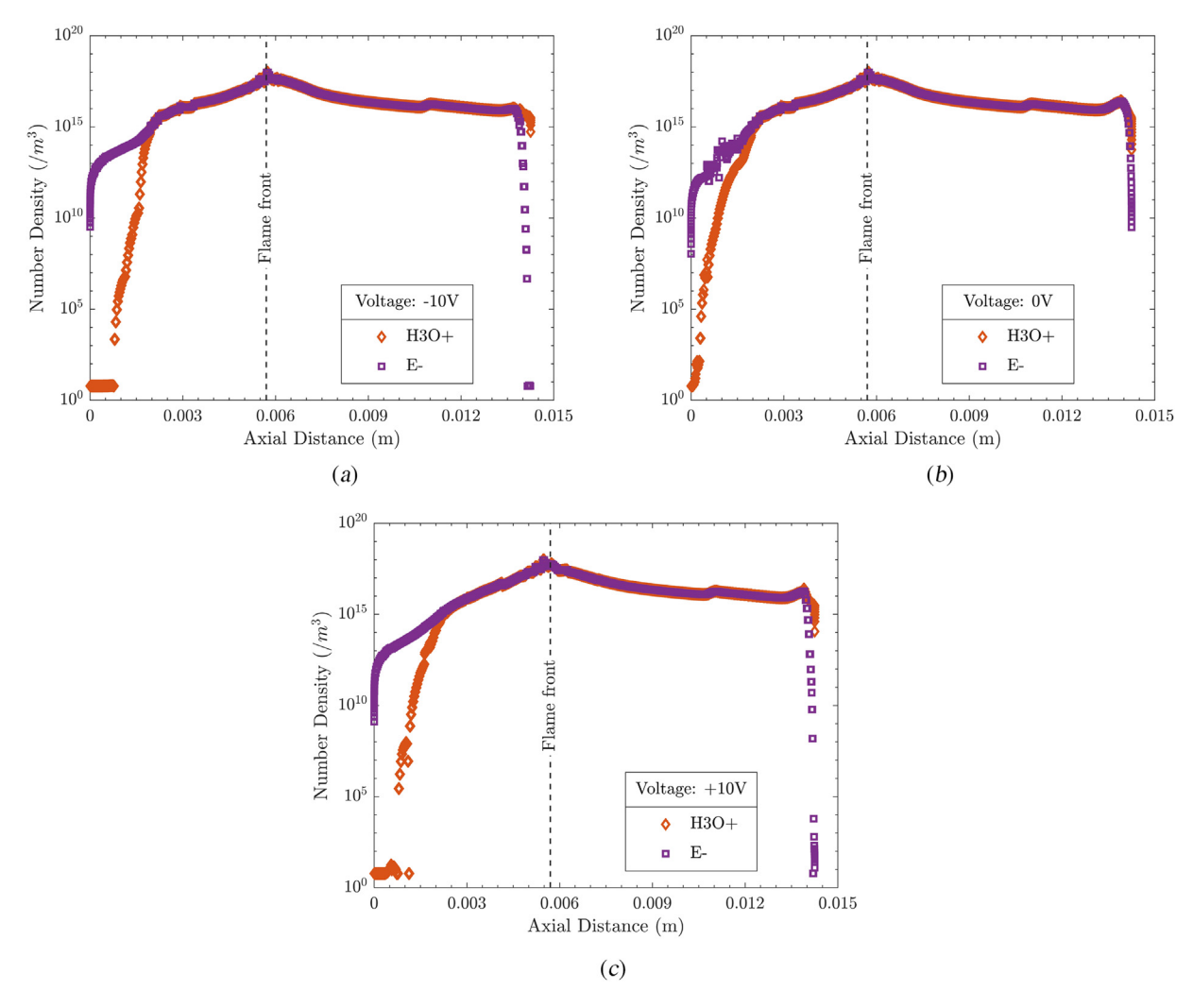
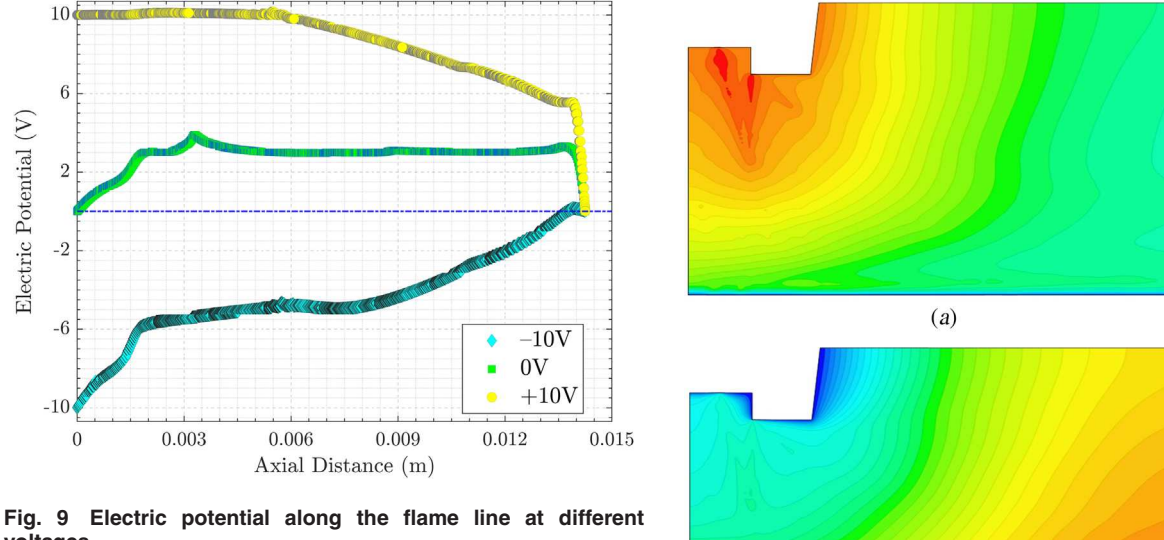


Fig. 8 Number density axial distribution: (a) -10 V, (b) 0V, and (c) +10 V



voltages

when  $+10 \,\mathrm{V}$  is applied at the torch tip, it can be observed that the electric potential does not decrease proportionately due to the presence of high density of the electrical species. However, for a negative voltage of  $-10 \,\mathrm{V}$ , the gradients are perceivable near the work surface as shown in Fig. 10(b). This is known as 'saturation'.

Fig. 10 Contour plot of Electric potential over the domain: (a) + 10 V and (b) - 10 V

(b)

5.62

The more mobile of the two charge carriers  $(e^-)$  vacates the region near the negative surface, growing the sheath, and the only means to further increase current is to increase the transport of the less mobile  $(H_3O^+)$  through the sheath. However, that happens very slowly compared to  $e^-$  so the current only increases very slowly with voltage.

**Current Density.** The ion and electron current densities are extracted for the upstream boundary based on different torch voltages and are calculated by Eqs. (30) and (31). In simulating the response of flames subject to an electric field, an accurate prediction of current densities is imperative. The cross-sectional average current densities do not change throughout the domain by virtue of Kirchoff's law, however, the cross-sectional average flux of individual species can vary. In the inner cone where ion densities are very high, both electrons and ions will have their peak current densities. As can be seen in Fig. 11, there is a hint of the onset of saturation in the current density plots. However, the ion current does not go to zero at positive voltage, meaning that a recirculation is delivering positive ions to the torch tip.

To further investigate this prospect, axial variation of equivalence ratio is considered. Since the F/O ratio is at 0.833 (volumetric), the tentative equivalence ratio is 1.6, denoting a rich flame. Therefore, there is more fuel than there is oxygen to burn it. This is done because the maximum flame temperature occurs at rich conditions, and that effect is severely exaggerated in atmospheric flames without nitrogen diluent. Entrained oxygen from the surrounding air helps complete combustion at the plate surface. It can be noted from Fig. 12 that once the reaction starts,  $CH_4$  isn't the only fuel and  $O_2$  isn't the only oxidizer. The combustion will result in different species and radicals as well. The oxygen will be consumed first, and there will be leftover fuel. However, there should not be much of the original reactants left once in the outer cone. The bulk of the flow will be intermediate species.

It is known [41,53,54] that the primary abundant cation will be  ${\rm H_3O^+}$  and is produced by the HCO<sup>+</sup> proton transfer reaction

$$CH + O \iff HCO^+ + e^-$$
 (R1)

$$HCO^{+} + H_{2}O \Longleftrightarrow H_{3}O^{+} + CO$$
 (R2)

Now, for steel surface, when carbon diffuses out of the work surface, it will then evaporate into the flame to form ions

$$H_3O^+ + C \iff HCO^+ + H_2$$
 (R3)

$$HCO^{+} + C_{2}H_{5}OH \iff H_{3}O^{+} + CO + C_{2}H_{4}$$
 (R4)

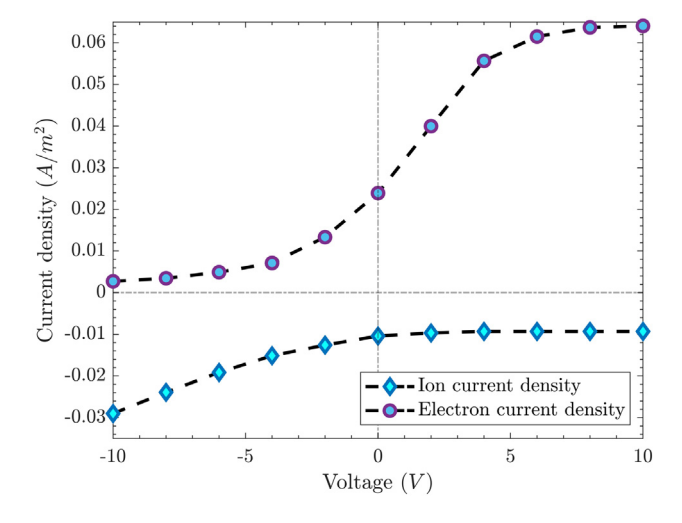


Fig. 11 Current densities at upstream boundary

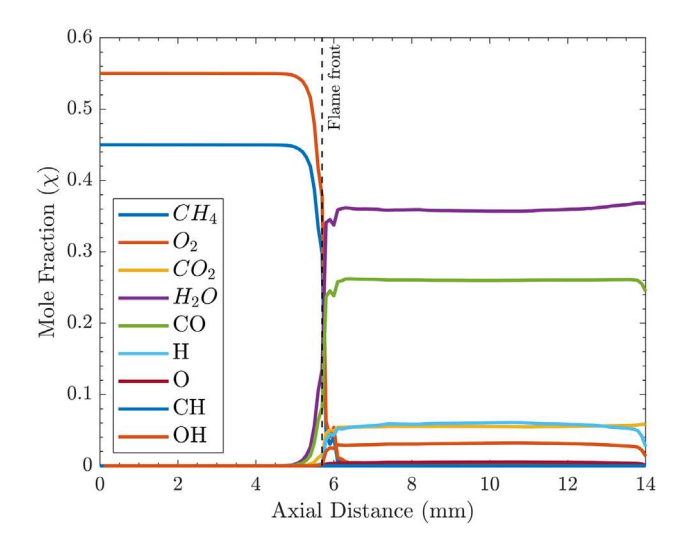


Fig. 12 Mole fractions of species distributed axially

Even though HCO $^+$  does not persist in considerable quantities outside of the flame, this is a vital species in the mechanism for the formation of other ions [2,14,55]. As a result, HCO $^+$  will contribute much to the production rate of  $H_3O^+$  ion, with Reaction (R4) taken from [56]. This is illustrated in Fig. 13. As can be seen, there is a notable spike in production rate of  $H_3O^+$  at an axial distance of  $\approx 10mm$  from the torch tip. Additionally, Prager et al. [54] showed that the consumption reactions for  $H_3O^+$  may be propagation reactions in the flame zone and recombination reactions

$$H_3O^+ + C_2H_2 \Longleftrightarrow C_2H_3O^+ + H_2 \tag{R5}$$

$$H_3O^+ + e^- \iff neutrals$$
 (R6)

Additional  $H_3O^+$  along with the oxygenated cation,  $C_2H_3O^+$  account for the recirculation of positive ions to the torch tip resulting in an ion current density lower than zero for the positive voltage regime as shown in Fig. 11.

**Current-Voltage** (i- $\nu$ ) **Characteristics.** The ion current density and the electron current density are integrated over the work surface to calculate the total electric current. Figure 14 presents the current-voltage (i- $\nu$ ) characteristics for the premixed oxyfuel flame subject to an electric field. The i- $\nu$  curve adopts three distinct regimes for different electric bias voltages applied.

- (i) **Regime1: Negative Saturation.** The region at the torch tip is starved of electrons, so currents have to be carried by heavy positive ions being driven upstream against the flow. Regime 1 appears when there is a sufficient growth in negative currents. It is evident from Fig. 14 the current for both copper and steel surfaces changes linearly with an almost perfect agreement. However, this segment characteristic is strongly governed by the F/O ratio [11].
- (ii) **Regime2: Ohmic.** In this slim regime, no saturation occurs, thus the name 'Ohmic', and both current densities follow Ohm's law. The availability of both positive and negative charge carriers is abundant in this regime. This narrow region acts as a zone where the current rapidly transitions between the two saturation regimes (regimes 1 and 3). While Ohmic behavior is present in all regimes, regime 2 has the most influence. The slope of the curve of regime 2 (or, Ohmic regime resistance) is sensitive to the F/O ratio, with a constant sensitivity with respect to the standoff distance.

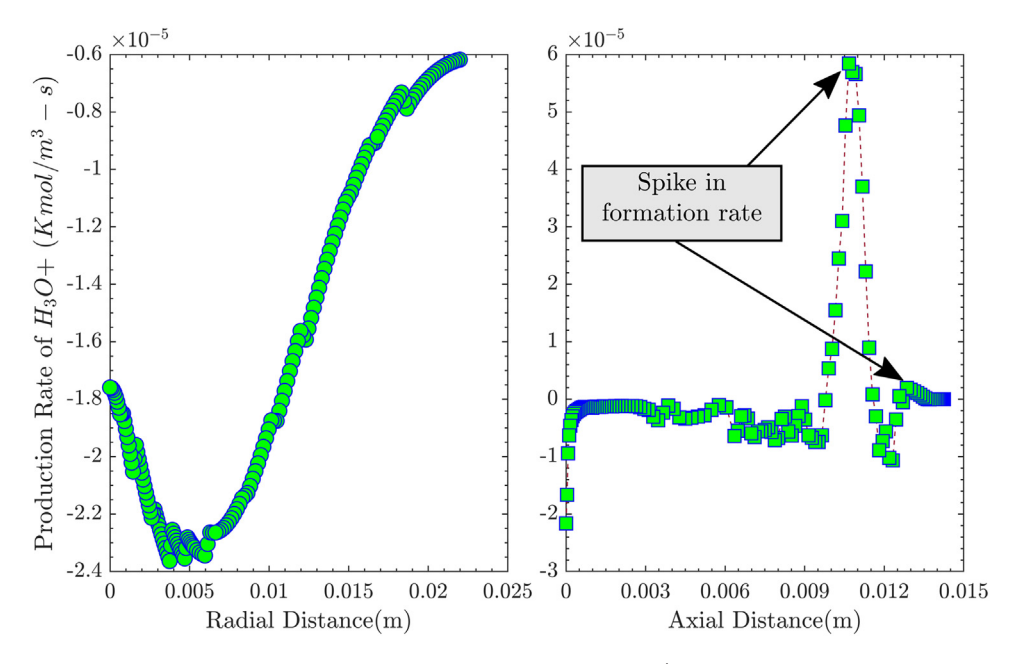


Fig. 13 Production rate of H<sub>3</sub>O<sup>+</sup>

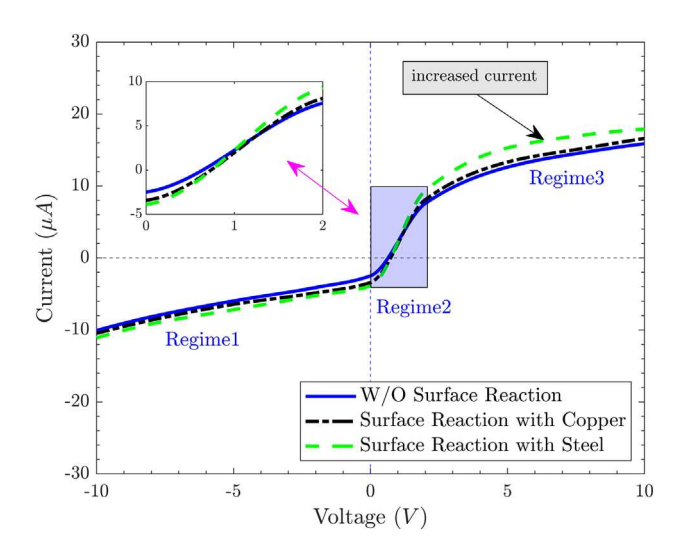


Fig. 14 *i-v* characteristics of oxyfuel flame subject to electric bias voltages

(iii) **Regime3: Positive Saturation.** Regime 3 appears when the positive current sufficiently grows, and when voltages are sufficiently positive to saturate the downstream sheath, meaning the electrical current there is due to the delivery of positive charge. Figure 14 shows that copper surfaces experience a stable and repeatable *i-v* characteristics in regime 3. This is because copper oxide is mechanically stable, and its melting temperature is higher than copper. It forms a stable protective layer over the metal and that halts chemical activity at the surface. Meanwhile, steel surface exhibits unrepeatable *i-v* characteristics with sporadically enhanced current in the same regime and drift in the floating potential.

At this juncture, the food for thought is, whether the enhanced currents in regime 3 for steel surface could somehow be a byproduct of the oxidation reaction itself? Oxidation is ruled out as the cause of the increased currents because the direction of electrical current is backwards, and a mechanism for the formation of free ions was not perceived. The additional positive ions generated due to the diffusion of carbon (from steel surface) in the flame are

delivered to the torch tip through a recirculation. What if that carbon is also generating additional ions over the work surface?

For a F/O ratio of 0.833 ( $\varphi \approx 1.6$ ), we have a rich flame and Jones et al. [57] showed that in addition to  $H_3O^+$  ions, the next dominant ion is  $C_3H_3^+$  once  $\varphi \approx 1.8-2.0$ . Production of  $C_3H_3^+$  ion includes two chemi-ionization reactions [58–60]

$$CH + O \iff HCO^+ + e^-$$
 (R7)

$$CH^* + C_2H_2 \Longleftrightarrow C_3H_3^+ + e^-$$
 (R8)

When a lean-stoichiometric flame is considered, meaning abundant O, Reaction (R7) is dominant [54,61], whereas Reaction (R8) presides when C<sub>2</sub>H<sub>2</sub> is ample [60,62].

Once in the flame, pure carbon diffusing out of the steel surface will react quickly  $(H_3O^+ + C \iff HCO^+ + H_2)$  and brings about  $HCO^+$  ions, subsequently generating  $H_3O^+$  ions. Hence, according to Eraslan et al. [63], with the presence of  $CH_2$ ,  $HCO^+$ , and  $H_3O^+$  will react to form  $CH_3^+$ , and consequently,  $C_3H_3^+$  ions

$$HCO^{+} + CH_{2} \Longleftrightarrow CH_{3}^{+} + CO$$
 (R9)

$$H_3O^+ + CH_2 \iff CH_3^+ + H_2O$$
 (R10)

$$CH_3^+ + C_2H_2 \iff C_3H_3^+ + H_2$$
 (R11)

Figure 15 presents the radial distribution of the reaction rate (R11) in vicinity of the work surface ( $\sim\!0.4\,\mathrm{mm}$ ). The spikes in reaction rate as shown in the figure portray the fact that when carbon diffuses out of the steel surface, chemi-ion such as  $C_2H_3O^+$  is obtained in addition to the higher production of  $H_3O^+$ . In the post-flame zone,  $C_3H_3^+$  reacts to form following cation [64]

$$C_3{H_3}^+ + H_2O \Longleftrightarrow C_2H_3O^+ + CH_2 \tag{R12} \label{eq:R12}$$

$$C_3H_3^+ + e^- \iff C_3H_2 + H$$
 (R13)

The additional cations generated through carbon diffusing out of the steel workpiece provide a recirculation of positive ions to the torch tip and increase net electric current in regime 3 of the i- $\nu$  curve due to the presence of those ions.

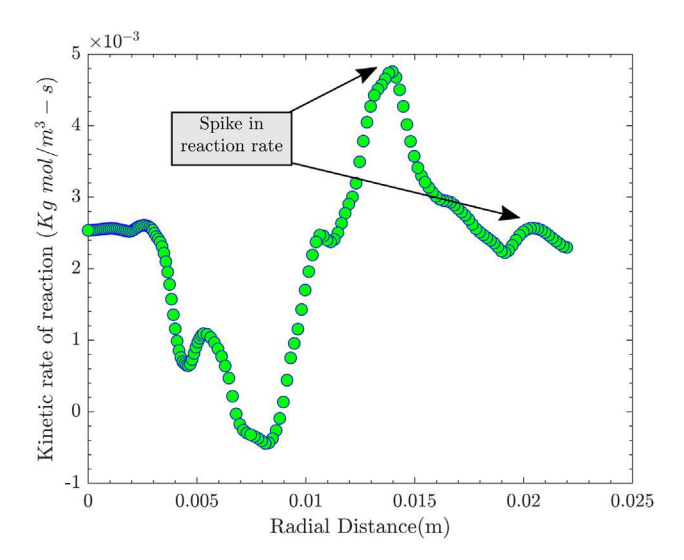


Fig. 15 Kinetic rate of reaction

### **Model Validation**

An experimental investigation was undertaken by Martin et al. [24]. This investigation was conducted using two experiments. In the first, ferrous wires with varying carbon content were burned while holding all other conditions constant. In the second, carbon was added directly by blowing fluidized graphite powder into the flame. The outcomes are shown in Fig. 16.

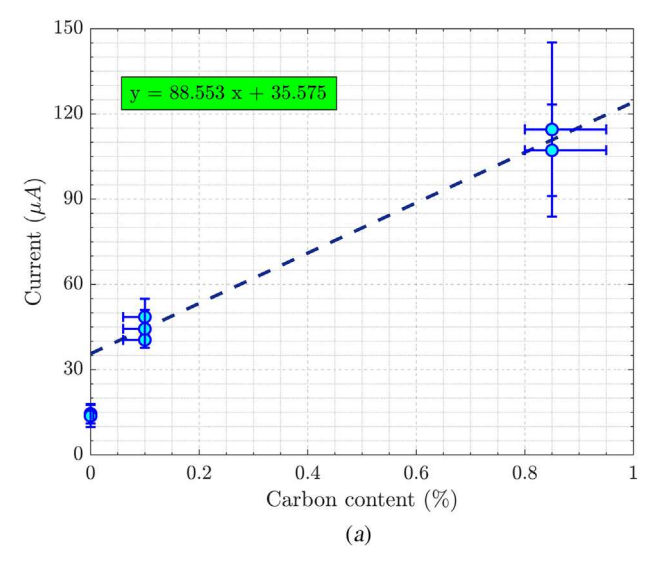
Figure 16(*a*) shows the variation of net current when carbon content is varied using different wires. Vertical error bars represent the maximum and minimum of the windowed mean value throughout the test. Horizontal error bars represent the most extreme variation in carbon content permissible by the material specification. It was concluded that the addition of even trace amounts of carbon in the outer cone (regardless of the source) can be expected to roughly double the positive saturation current.

Current signals for various mass flow rates of graphite are shown in Fig. 16(b). The points represent the mean signal, vertical error bars are constructed from rms noise, and horizontal error bars represent a 95% confidence interval on the mass flowrate measurement. There is good confidence that the trend is linear. Despite the rms signal amplitude and the mass measurement uncertainty, the mean values rise linearly with little scatter. The extreme current was found to be repeatable, though a clean signal with stainless steel wire was never achieved at this feed rate.

The resulting i- $\nu$  curves for the experimental investigation are compared with the computational results and are shown in Figs. 17(a)–17(b). The experimental results were taken for volumetric flow rates of 20 scfh and 25 scfh, respectively, whereas the computational result corresponds to an inlet velocity of  $12 \text{ ms}^{-1}$ . The reason there is so much scatter for the experimental curves is because the standoff is high (= 12.7 mm), and the signals are so small. This is only about  $5\mu A$  of current in regime 3, which is very small. At lower standoffs, the work will be in a region with more ions, so the signals are much stronger. When the flame is moved off the edge of a plate/work surface, the current is not significantly changed until more than half of the flame is off the work. This suggests that the electrical resistance of the outer cone is more or less uniform, and the current can enter virtually any part of the cone.

It can be readily observed from the figures that, while regime 1 matches linearly for both experimental and computational model, a degree of variation can be seen in regime 3. However, at the same time, the variation is compromised by increasing the volumetric flowrate from 20 scfh to 25 scfh. The probable grounds for such variation in the *i-v* plots could be due to:

 The initial velocity prescribed at the inlet might not be approximating the physical flow rates perfectly. Regime 3



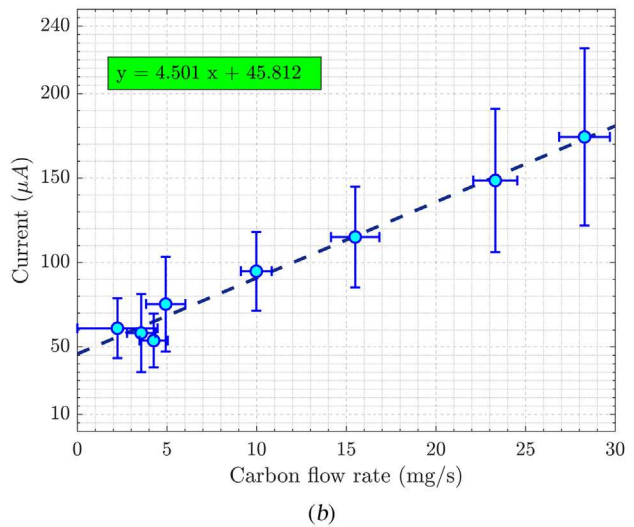


Fig. 16 Current signals measured for different carbon contents and mass flow rates: (a) carbon content (%) and (b) carbon flowrate (mg/s)

is quite sensitive to the velocity. Decreasing the velocity will tend to decrease regime 3 current. It may also slightly increase regime 1 current; however, those data seem to be relatively insensitive to flow rate; they are much more sensitive to F/O ratio.

- (ii) The ions' mobility might be more substantial than the values assigned in the computational model. Because the mobility is quite small, the recombination rate has a bigger part to play in regime 3. In this regime, all of the electrons are driven away from the work, so the current is determined by the number of ions that survive to reach the plate. It is still weakly sensitive to voltage because the 'sheath' where electrons are absent grows deeper into the flame, where ions are more abundant, so more survive to reach the work.
- (iii) A lower velocity in the hot zone gives ions more time to recombine before they reach the work surface. This results in lower ion concentrations and lower saturation currents.

# Conclusions

A two-dimensional model has been developed using the ANSYS FLUENT CFD code and is capable of analyzing the

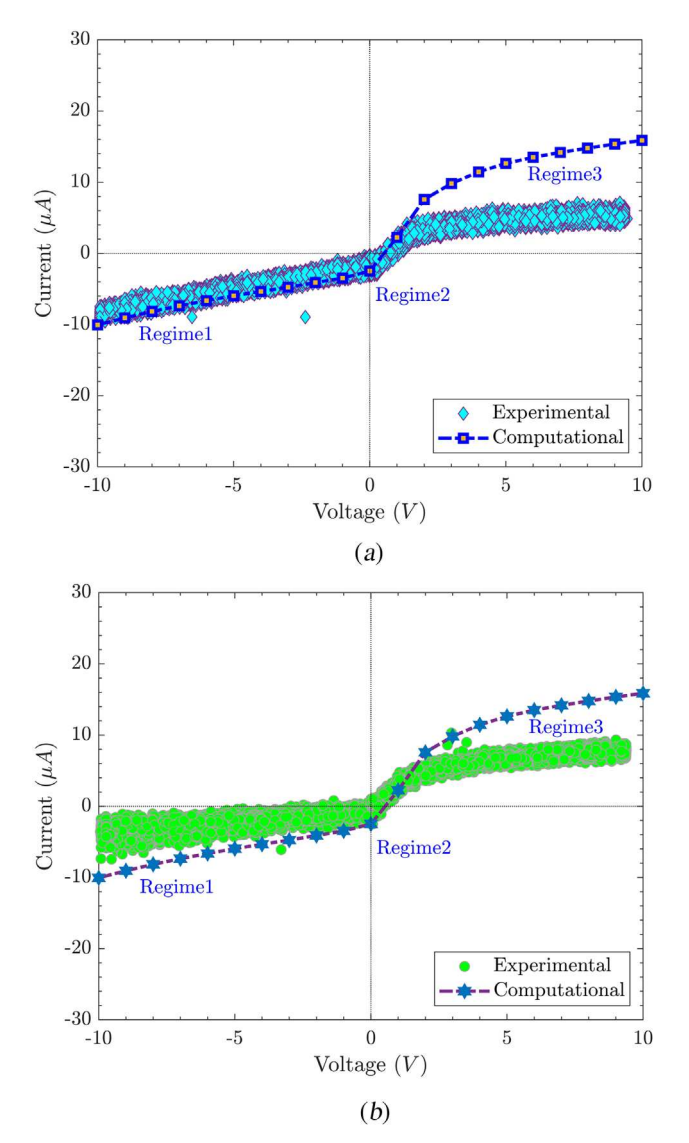


Fig. 17 Validating i-v characteristics for different flow rates: (a) 20 scfh and (b) 25 scfh

transportation of electrons' and ions' in a premixed CH<sub>4</sub>-O<sub>2</sub> flame subject to electric bias voltages. This essentially imitates the preheating stage of oxyfuel flame-cutting process. The CFD solver on FLUENT was incorporated with a chemical kinetic mechanism and transport property evaluations. The simulations provided reasonable outcomes of the combustion and electrochemical properties. The transport results illustrate the current-voltage (i-v)relationship. Primarily, the role of secondary ions on the i-v relationship has been investigated and have been compared to the physical experiment. The aforementioned results permit following

- (i) A source term of gaseous carbon has been assigned at the work surface (surface 4) for steel that 'mimics' the surface reaction phenomena.
- (ii) Secondary ions in the oxyfuel-cutting flame are produced in part (if not entirely) by carbon.
- (iii) Ion current density experiences a recirculation that delivers positive ions to the torch tip.
- (iv) Sporadically enhanced electric currents observed in the positive saturation are due to the additional ions generated by carbon reaction. Once in the flame, pure carbon reacts quickly to form ions.

(v) Some degree of difference has been observed in the i-v relationship, however, this can be compromised by playing around with the process parameters such as inlet velocity, F/O ratio, standoff distance, etc.

### **Funding Data**

• National Science Foundation (NSF) (Grant Nos. 1900540 and 1900698; Funder ID: 10.13039/100000001).

### **Conflict of Interest**

The authors declare that they have no known competing financial interests or personal relationships that could have appeared to influence the work reported in this paper.

### **Nomenclature**

 $A = area (m^2)$ 

 $c_i = \text{molar concentration of species i (kmol m}^{-3})$ 

 $D_i = \text{diffusivity of species } i \text{ (m}^2 \text{ s}^{-1})$ 

 $E_a$  = activation energy (J mol<sup>-1</sup>) K = mobility (m<sup>2</sup> V<sup>-1</sup> s<sup>-1</sup>)

k = rate constant

 $n_i$  = number density of species i (m<sup>-3</sup>)

 $q_e$  = fundamental charge (1.6E-19) (C)

 $Q = \text{volumetric flow rate (m}^3/\text{s)}$   $R_u = \text{gas constant (J mol}^{-1} \text{ K}^{-1})$ 

 $Sc_t = \text{turbulent Schmidt number}$ 

t = time(S)

T = temperature (K)

 $U = velocity (ms^{-1})$ 

 $Y_i = \text{mass fraction of species } i$ 

 $y^{+}$  = dimensionless wall distance

 $\varepsilon_0$  = vacuum permittivity (8.9E-12) (C V<sup>-1</sup> m<sup>-1</sup>)

 $\lambda_D$  = Debye length ( $\mu$ m)

 $\sigma_i$  = space charge density of species i (C m<sup>-3</sup>)

 $_B = \text{Boltzmann constant} (1.3\text{\&E}-23) (\text{J K}^{-1})$ 

 $\beta$  = temperature exponent

 $\mu = \text{dynamic viscosity (Pa} \cdot \text{s})$ 

 $\rho = \text{density (kg/m}^3)$ 

 $\tau = \text{stress tensor} (\text{N/m}^2)$ 

# Appendix: Grid Convergence Index

A grid convergence study was performed to compute the numerical uncertainty of the computational model. The grid convergence index (GCI) method [65], based on Richardson extrapolation (RE), was chosen to estimate the discretization error within each grid. GCI is a well-known approach to compute grid uncertainty and the articles from [66-70] illustrate the applications of the same.

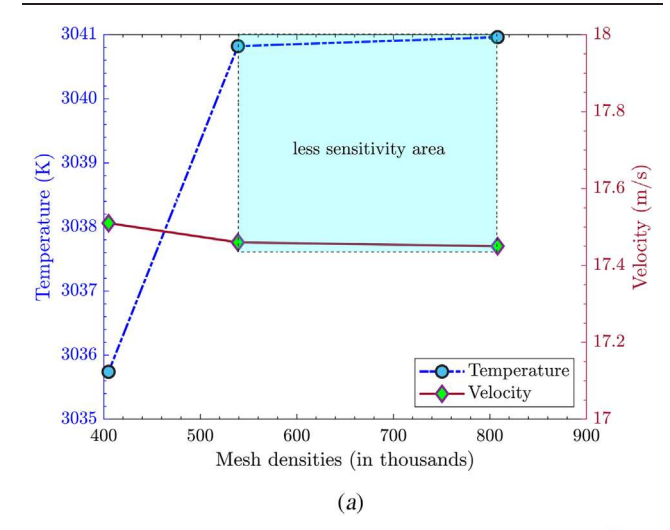
In this study, three different structured grids were examined, formed by quadrilateral grid elements. Table 7 presents the grid converge index results for the three grids examined, with pictorial illustrations in Fig. 18. It is evident from both the table and figures that the results do not vary significantly as the mesh density goes from  $\approx 539$  thousands to  $\approx 808$  thousands. Thereby, for the analysis of the current computational model, a mesh density with 539,076 nodes and 537,500 elements was considered.

For the electrical transport part, since the ions and electrons have different number densities near the surface, the Debye length [6,31] is calculated to check whether the meshes are fully resolving the electrical species.

$$\lambda_D = \sqrt{\frac{\frac{\varepsilon_0 k_B}{q_e^2}}{\frac{n_e}{T_e} + \sum_{i}^{N} \frac{z_i^2 n_i}{T_i}}}$$
(A1)

Table 7 Grid convergence index

Critical parameters	Case-A	Case-B	Case-C	Unit
Mesh densities Temperature, T Velocity, U Electric potential, P Number density, N GCI <sub>fine</sub> : T GCI <sub>fine</sub> : U GCI <sub>fine</sub> : P GCI <sub>fine</sub> : N	$4053035.5717.5110.849.60 × 10^{17}$	539 3040.74 17.46 10.64 9.62 × 10 <sup>17</sup> 9.034e-04% 2.178e-02% 1.293e-02% 1.514e-03%	808 3040.96 17.45 10.63 9.62 × 10 <sup>17</sup>	thousands K ms <sup>-1</sup> V /m <sup>3</sup>



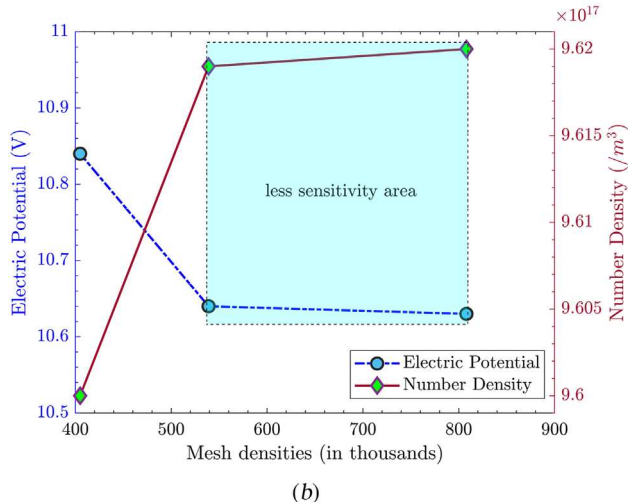


Fig. 18 Grid convergence study: (a) combustion part and (b) electrochemical part

where  $\lambda_D$  is the Debye length,  $\varepsilon_0$  is the permittivity of free space,  $k_B$  is Boltzmann's constant, which is 1.380649 × 10<sup>23</sup> J/K,  $q_e$  is the electrical charge of a particle, which is  $1.602 \times 10^{-19}$  coulombs,  $n_e$  is the density of electrons,  $T_e$  is the temperature of the electrons,  $z_i$  is the rate of ionic charge compared to the charge of electrons,  $n_i$  is the density of atomic species i, and  $T_i$  is the temperature of ions. The temperature of electrons and ions are assumed equal to the flame temperature  $(T_e \approx T)$  from Clements and Smy's approximation [71,72]. With the current mesh density, the value of  $\lambda_D$  obtained was well within the experimental observations,  $3.8 - 38 \,\mu m$  [26].

### References

[1] Wilson, H., 1916, "The Electrical Conductivity and Luminosity of Flames Containing Salt Vapours," Phil. Trans. R. Soc. Lond., 216, pp. 63-90.

- [2] Calcote, H. F., 1961, "Ion Production and Recombination in Flames," Symp. (Int.) Combust., 8(1), pp. 184–199.
- [3] Han, J., Belhi, M., Casey, T. A., Bisetti, F., Im, H. G., and Chen, J.-Y., 2017, "The i-v Curve Characteristics of Burner-Stabilized Premixed Flames: Detailed and Reduced Models," Proc. Combust. Inst., 36(1), pp. 1241–1250.
- [4] Pond, T. L., and Martin, C. R., 2020, "Electrical Characteristics of the Oxyfuel Flame While Cutting Steel," Exp. Therm. Fluid Sci., 112, p. 109985.
- [5] Martin, C. R., Untaroiu, A., Xu, K., and Mahbobur Raman, S. M., 2022, "A Study of the Efficacy of Flame Electrical Resistance for Standoff Measurements During the Oxyfuel Cutting Process," ASME J. Manuf. Sci. Eng., 144(7),
- [6] Martin, C. R., 2018, "A Study of Ion Currents in an Oxyfuel Flame Due to Work Surface Chemical Action," Exp. Therm. Fluid Sci., 98, pp.
- [7] Goodings, J. M., Guo, J., Hayhurst, A. N., and Taylor, S. G., 2001, 'Current-Voltage Characteristics in a Flame Plasma: Analysis for Positive and Negative Ions, With Applications," Int. J. Mass Spectrom., 206(1-2), pp.
- [8] Karnani, S., and Dunn-Rankin, D., 2015, "Detailed Characterization of dc Electric Field Effects on Small Non-Premixed Flames," Combust, Flame, 162(7), pp. 2865-2872.
- [9] Imamura, O., Chen, B., Nishida, S., Yamashita, K., Tsue, M., and Kono, M., 2011, "Combustion of Ethanol Fuel Droplet in Vertical Direct Current Electric Field," Proc. Combust. Inst., 33(2), pp. 2005-2011.
- [10] Speelman, N., de Goey, L. P. H., and van Oijen, J. A., 2015, "Development of a Numerical Model for the Electric Current in Burner-Stabilised Methane-Air Flames," Combust. Theory Modell., 19(2), pp. 159–187.
- [11] Martin, C. R., Leonard, C., and VonFricken, J., 2017, "A Study of the Electrical
- Characteristics of an Oxy-Fuel Flame," Exp. Therm. Fluid Sci., 88, pp. 65–72. [12] Luo, Y., Gan, Y., and Jiang, Z., 2020, "Study on the Electrical Response of Small Ethanol-Air Diffusion Flame Under the Uniform Electric Field," Int. J. Energy Res., 44(14), pp. 11872-11882.
- [13] Lawton, J., and Weinberg, F. J., 1969, Electrical Aspects of Combustion, Clarendon Press, Oxford.
- [14] Fialkov, A. B., 1997, "Investigations on Ions in Flames," Prog. Energy Combust. Sci., 23(5-6), pp. 399-528.
- [15] Xu, K., Untaroiu, A., and Martin, C. R., 2021, "Simulation of Ion Current in Oxyfuel Flame Subject to an Electric Field," ASME Paper No. IMECE2020-
- [16] Grosse, A. V., and Conway, J. B., 1958, "Combustion of Metals in Oxygen," Ind. Eng. Chem., 50(4), pp. 663-672.
- [17] Bolobov, V. I., 2001, "Conditions for Ignition of Iron and Carbon Steel in Oxygen," Combust., Explos. Shock Waves, 37(3), pp. 292-296.
- [18] Miesse, C. M., Masel, R. I., Jensen, C. D., Shannon, M. A., and Short, M., 2004, "Submillimeter-Scale Combustion," AIChE J., 50(12), pp. 3206-3214.
- [19] Saiki, Y., Fan, Y., and Suzuki, Y., 2015, "Radical Quenching of Metal Wall Surface in a Methane-Air Premixed Flame," Combust. Flame, 162(10), pp. 4036-4045.
- [20] Vlachos, D. G., Schmidt, L. D., and Aris, R., 1993, "Ignition and Extinction of Flames Near Surfaces: Combustion of  $H_2$  in Air," Combust. Flame, 95(3), pp. 313-335
- [21] Vlachos, D. G., Schmidt, L. D., and Aris, R., 1994, "Ignition and Extinction of Flames Near Surfaces: Combustion of CH<sub>4</sub> in Air," Combust. Flame, 40(6), pp. 1005-1017.
- [22] Narukawa, K., Minamoto, Y., Shimura, M., and Tanahashi, M., 2020, "Near-Wall Flame Propagation Behaviour With and Without Surface Reactions," Fuel, 268, p. 117216.
- [23] Salimath, P. S., Ertesvåg, I. S., and Gruber, A., 2020, "Computational Analysis of Premixed Methane-Air Flame Interacting With a Solid Wall or a Hydrogen Porous Wall," Fuel, 272, p. 117658.
- [24] Martin, C. R., Oswald, D., Rahman, S. M. M., and Untaroiu, A., 2023, "Ions in the Oxyfuel Cutting Flame Due to Workpiece Carbon," Manuf. Lett., Press, 36, pp. 22-25.
- Yamashita, K., Karnani, S., and Dunn-Rankin, D., 2009, "Numerical Prediction of Ion Current From a Small Methane Jet Flame," Combust. Flame, 156(6), pp. 1227-1233
- [26] Martin, C. R., Untaroiu, A., and Xu, K., 2022, "Spatially Resolved Ion Density Measurements in an Oxyfuel Cutting Flame," Combust. Sci. Technol., 194(5),
- [27] Peters, N., 2000, Turbulent Combustion, Cambridge University Press, Cambridge, UK.
- [28] Andrews, G. E., and Bradley, D., 1972, "The Burning Velocity of Methane-Air Mixtures," Combust. Flame, 19(2), pp. 275–288.
  [29] Bibrzycki, J., and Poinsot, T., 2010, "Investigation of Laminar Flame Speed of
- CH<sub>4</sub>/N<sub>2</sub>/O<sub>2</sub> and CH<sub>4</sub>/CO<sub>2</sub>/O<sub>2</sub> Mixtures Using Reduced Chemical Kinetic Mechanisms," Archivum Combustionis, 30(4), pp. 287-296.
- [30] Goodwin, D. G., Moffat, H. K., and Speth, R. L., 2015, "Cantera: An Object-Oriented Software Toolkit for Chemical Kinetics, Thermodynamics, and Transport Processes," Version 2.2.0, Zenodo.
- [31] Xu, K., 2021, "Simulation of Electrical Characteristics in Oxyfuel Flame Subject to an Electric Field," Master's thesis, Virginia Tech, Blacksburg, VA.
- [32] Martin, C. R., Untaroiu, A., and Xu, K., 2021, "A One-Dimensional Model for Ion Transport in a Flame With Two Absorbing Surfaces," Combust. Theory Modell., **25**(1), pp. 22–43.
- [33] Kobayashi, H., Kawabata, Y., and Maruta, K., 1998, "Experimental Study on General Correlation of Turbulent Burning Velocity at High Pressure," Symp. (Int.) Combust., 27(1), pp. 941-948.

- [34] Kobayashi, H., and Kawazoe, H., 2000, "Flame Instability Effects on the Smallest Wrinkling Scale and Burning Velocity of High-Pressure Turbulent Premixed Flames," Proc. Combust. Inst., 28(1), pp. 375–382.
- [35] Rockwell, S. R., and Rangwala, A. S., 2013, "Influence of Coal Dust on Pre-mixed Turbulent Methane–Air Flames," Combust. Flame, 160(3), pp. 635–640.
- [36] Poinsot, T., and Veynante, D., 2005, Theoretical and Numerical Combustion, R.T. Edwards, Inc., Philadelphia, PA.
- [37] ANSYS Fluent user's guide, 2013, ANSYS FLUENT 12.0 User's Guide (enea.it), ANSYS Inc., Canonsburg, PA.
- [38] Shih, T. H., Liou, W. W., Shabbir, A., Yang, Z., and Zhu, J., 1995, "A New  $k-\in$  Eddy Viscosity Model for High Reynolds Number Turbulent Flows," Comput. Fluids, 24(3), pp. 227-238.
- [39] Hinze, J. O., 1975, Turbulence, McGraw-Hill Publishing Co, New York.
- [40] Smith, G. P., Golden, D. M., Frenklach, M., Moriarty, N. W., Eiteneer, B., Goldenberg, M., Bowman, C. T., Hanson, R. K., Song, S., Gardiner, W. C., Jr., Lissianski, V. V., and Qin, Z., 1999, "GRI-Mech 3.0," Berkeley, CA, accessed Nov 11, 2022, http://www.me. berkeley.edu/gri\_mech/
- [41] Belhi, M., Domingo, P., and Vervisch, P., 2010, "Direct Numerical Simulation of the Effect of an Electric Field on Flame Stability," Combust. Flame, 157(12), pp. 2286–2297.
- [42] Burcat, A., 2006, "Ideal Gas Thermodynamic Data in Polynomial Form for Combustion and Air Pollution Use," Budapest, Hungary, accessed Nov 11, 2022, http://garfield.chem.elte.hu/Burcat/burcat.html
- [43] Chen, B., Wang, H., Wang, Z., Han, J., Alquaity, A. B. S., Wang, H., Hansen, N., and Sarathy, S. M., 2019, "Ion Chemistry in Premixed Rich Methane Flames," Combust. Flame, 202, pp. 208-218.
- [44] Belhi, M., Lee, B. J., Cha, M. S., and Im, H. G., 2019, "Three-Dimensional Simulation of Ionic Wind in a Laminar Premixed Bunsen Flame Subjected to a Transverse DC Electric Field," Combust. Flame, 202, pp. 90-106.
- [45] Belhi, M., Lee, B. J., Bisetti, F., and Im, H. G., 2017, "A Computational Study of the Effects of DC Electric Fields on Non-Premixed Counterflow Methane-Air Flames," J. Phys. D: Appl. Phys., **50**(49), p. 494005.
- [46] Rahman, S. M. M., Karim, K. E., and Simanto, M. H. S., 2016, "Effect of Heat Treatment on Low Carbon Steel: An Experimental Investigation," Appl. Mech. Mater., 860, pp. 7-12.
- [47] Rumble, J. R., 2017, CRC Handbook of Chemistry and Physics, CRC Press, Boca Raton, FL, USA.
- [48] Material Property Data, "Material Property Data," accessed Nov 11, 2022, https://matweb.com/
- [49] Liu, B. J. D., and Pope, S. B., 2005, "The Performance of in Situ Adaptive Tabulation in Computations of Turbulent Flames," Combust. Theory Model., 9(4),
- [50] Kim, D., Rizzi, F., Cheng, K. W., Han, J., Bisetti, F., and Knio, O. M., 2015, "Uncertainty Quantification of Ion Chemistry in Lean and Stoichiometric Homogenous Mixtures of Methane, Oxygen, and Argon," Combust. Flame, 162(7), pp. 2904–2915.
- [51] Boucher, P. E., 1928, "The Drop of Potential at the Cathode in Flames," Phys. Rev., 31(5), pp. 833-850.
- [52] Han, J., Belhi, M., Bisetti, F., and Sarathy, S. M., 2015, "Numerical Modelling of Ion Transport in Flames," Combust. Theory Modell., 19(6), pp. 744-772.
- [53] Green, J. A., and Sugden, T. M., 1963, "Some Observations on the Mechanism of Ionization in Flames Containing Hydrocarbons," Symp. (Int.) Combust., 9(1), pp. 607-621.

- [54] Prager, J., Riedel, U., and Warnatz, J., 2007, "Modeling Ion Chemistry and Charged Species Diffusion in Lean Methane-Oxygen Flames," Proc. Combust. Inst., 31(1), pp. 1129–1137.
- [55] Calcote, H. F., 1963, "Ion and Electron Profiles in Flames," Symp. (Int.) Com-
- bust., 9(1), pp. 622–637.
  [56] McElroy, D., Walsh, C., Markwick, A., Cordiner, M., Smith, K., and Millar, T., 2013, "The UMIST Database for Astrochemistry," Astron. Astrophys., 550, p. A36.
- [57] Jones, H. R. N., and Hayhurst, A. N., 2016, "Measurements of the Concentrations of Positive and Negative Ions Along Premixed Fuel-Rich Flames of Methane and Oxygen," Combust. Flame, 166, pp. 86–97.
  [58] Deckers, J., and Tiggelen, A. V., 1958, "Ion Identification in Flames by Mass
- Spectrometry," Nature, 181(4621), pp. 1460-1460.
- [59] Deckers, J., and Tiggelen, A. V., 1958, "Identity of Ions in Some Flames," Nature, 182(4639), pp. 863-863.
- [60] Hayhurst, A. N., and Jones, H. R. N., 1982, "Chemi-Ionization in Oxyacetylene Flames," Nature, 296(5852), pp. 61-63.
- [61] Calcote, H. F., and Pease, R. N., 1951, "Electrical Properties of Flames: Burner Flames in Longitudinal Electric Fields," Ind. Eng. Chem., 43(12), pp. 2726-2731.
- [62] Hayhurst, A. N., and Jones, H. R. N., 1987, "Ions and Soot in Flames," J. Chem. Soc. Faraday Trans., 83(1), pp. 1–27.
- [63] Eraslan, A. N., and Brown, R. C., 1988, "Chemiionization and Ion-Molecule Reactions in Fuel-Rich Acetylene Flames," Combust. Flame, **74**(1), pp. 19–37.
- [64] Cancian, J., Bennett, B. A. V., Colket, M. B., and Smooke, M. D., 2013, "Prediction of Electron and Ion Concentrations in Low-Pressure Premixed Acetylene and Ethylene Flames," Combust. Theory Modell., 17(2), pp. 294-315.
- [65] Celik, I. B., Ghia, U., Roache, P. J., and Freitas, C. J., 2008, "Procedure for Estimation and Reporting of Uncertainty Due to Discretization in CFD Applications," ASME J. Fluids Eng., 130(7), p. 078001.
- Alam, M. D., and Soeimanikutanaei, S., 2022, "Effects of Geometrical Configuration on the Aerodynamic Performance of the Joined Wings," ASME Paper No. IMECE2021-72087.
- [67] Alam, M. D., and Cao, Y., 2021, "Static and Modal Analysis of a Crankshaft Reciprocating Driver for Reciprocating-Airfoil (RA) Driven VTOL Aircraft," Mechanics Based Design of Structures and Machines, Taylor & Francis, Boca Raton, FL, pp. 1-16.
- [68] Fu, G., and Untaroiu, A., 2021, "Investigation of Tire Rotating Modeling Techniques Using Computational Fluid Dynamics," ASME J. Fluids Eng., 143(11),
- [69] Hayden, A., and Untaroiu, A., 2022, "Strain Response and Aerodynamic Damping of a Swirl Distortion Generator Using Computational Fluid Dynamics, ASME J. Fluids Eng., 144(3), p. 031204.
- [70] Rahman, S. M. M., Warrier, R., Untaroiu, A., and Martin, C. R., 2022, "Electrical Characteristics of the Oxyfuel Preheat Flame: 3D Computational Model Subject to Electric Bias Voltages," ASME Paper No. IMECE2022-95787.
- Clements, R. M., and Smy, P. R., 1969, "Electrostatic-Probe Studies in a Flame Plasma," J. Appl. Phys., 40(11), pp. 4553–4558.
- [72] Clements, R. M., and Smy, P. R., 1970, "Ion Current From a Collision-Dominated Flowing Plasma to a Cylindrical Electrode Surrounded by a Thin Sheath," J. Appl. Phys., 41(9), pp. 3745-3749.